

# Learning Partial Differential Equations with Deep Parallel Neural Operator

Qinglong Ma<sup>a</sup>, Peizhi Zhao<sup>a</sup>, Sen Wang<sup>a</sup>, Tao Song<sup>a,\*</sup>

<sup>a</sup>*College of Computer Science and Technology, China University of Petroleum (East China), Qingdao, 266580, Shandong, China*

---

## Abstract

In recent years, Solving partial differential equations has shifted the focus of traditional neural network studies from finite-dimensional Euclidean spaces to generalized functional spaces in research. A novel methodology is to learn an operator as a means of approximating the mapping between outputs. Currently, researchers have proposed a variety of operator architectures. Nevertheless, the majority of these architectures adopt an iterative update architecture, whereby a single operator is learned from the same function space. In practical physical science problems, the numerical solutions of partial differential equations are complex, and a serial single operator is unable to accurately approximate the intricate mapping between input and output. So, We propose a deep parallel operator model (DPNO) for efficiently and accurately solving partial differential equations. DPNO employs convolutional neural networks to extract local features and map data into distinct latent spaces. Designing a parallel block of double Fourier neural operators to solve the iterative error problem. DPNO approximates complex mappings between inputs and outputs by learning multiple operators in different potential spaces in parallel blocks. DPNO achieved the best performance on five of them, with an average improvement of 11.6%, and ranked second on one dataset.

*Keywords:* Mechanical partial differential equations, neural operator, scientific machine learning, deep learning-based PDE solver

---

<sup>\*</sup>corresponding author

*Email address:* `tsong@upc.edu.cn` (Tao Song)

## 1. Introduction

In scientific and engineering fields, partial differential equations (PDEs) are commonly used to model phenomena in a variety of physical domains, such as fluid mechanics, mechanics of materials, quantum mechanics, and electricity. The vast majority of partial differential equations lack analytical solutions, such as the Navier-Stokes equation, making numerical methods the primary means of solving them [1, 2]. Although these methods are effective, they are computationally expensive and often require significant computing resources. Classical numerical methods often require some trade-off in accuracy while pursuing computational efficiency. Therefore, there is an urgent need to find a class of efficient solution methods.

In recent years, deep learning researchers have made significant progress, making it possible for AI to replace traditional numerical solvers and numerical simulators [3, 4, 5, 6]. Notably, the concept of neural operators and their innovative architectures have demonstrated considerable promise in approximating intricate mappings, with extensive research conducted in this area. This paradigm aims to approximate the mapping relationship between inputs and outputs by training deep models with innovative architectures. Specifically, it learns correlations in time series data. For example, predicting future flows and pressures based on information about flows and pressures at a point in time in the past [7]. In addition, the method is capable of directly learning the mapping relationship between different parameters. For example, the macroscopic mechanical properties of a composite are inferred from its microstructure [8]. This approach has shown exceptional performance in various fields, including fluid mechanics and material mechanics.

Fourier neural operators have proposed a novel solution that performs well in handling partial differential equation problems. It transforms the data into the Fourier domain for learning [9]. However, Fourier neural operators rely on the iterative update strategy of the operator, which can result in partial information loss during iterative calls. The main reason for this error accumulation is the frequent conversion between the spatial and spectral domains within different operational blocks, as well as negative multiplications performed inside the Fourier domain. In this process, some spatial information is lost due to the forward and backward transformations of spectral convolution. Therefore, the cumulative loss of spatial information in processing the same information after each iteration reduces its efficiency [10, 11].

For several classical partial differential equations in fluid mechanics, The

research in this paper focuses on developing a new operator architecture. The architecture uses Fast Fourier Transform (FFT) to learn partial differential equations. However, it solves the iterative error problem by using a clean and efficient parallel architecture. Our contributions are as follows:

- We propose a new neural operator architecture, the Deep Parallel Neural Operator. The overall architecture maps the raw data to different potential spaces after multiple encodings.
- We design a parallel operator block. It learns the input and output mappings of different potential spaces in parallel.
- We conduct six benchmark experiments to compare our model with benchmark models and currently recognized state-of-the-art models. Our model achieves the best results on five datasets with an average improvement of 11.6%, and ranks second on one dataset. In addition, we conduct an ablation study to compare the performance of parallel block with serial block. The results show an average performance improvement of 10.8% for parallel block.

## 2. Related work

### 2.1. Neural Operator

Neural operators are a series of methods for learning meshless, infinite-dimensional operators using neural networks that have been proposed in recent years of research. Neural operators solve the mesh dependence problem of finite-dimensional operator methods by generating a set of mesh parameters that can be used for different discretisations [12]. It has the ability to transfer solutions between arbitrary meshes. In addition, the neural operator needs to be trained only once, and the subsequent performances of various new instance parameters require only forward propagation calculations. This reduces the computational cost associated with repeated training. Neural operators are purely data-driven and do not rely on any prior knowledge about partial differential equations [13]. This makes it possible for the operator to learn solutions to partial differential equations.

Specifically, neural operators are described as an iterative update architecture:  $v_0 \rightarrow v_1 \rightarrow \dots \rightarrow v_T$ , Where  $v_j$  is a series of functions on  $\mathbb{R}^{d_v}$ . Input  $a \in A$  is first elevated to a higher dimensional representation through local transformation  $P$ :  $v_0(x) = P(a(x))$ . This local transformation is typically

parameterized by a shallow fully connected neural network. Then apply several updates and iterations:  $v_t \rightarrow v_{t+1}$ . The output  $u(x) = Q(v_T(x))$  is the projection of  $v_T$  through local transformation  $Q: \mathbb{R}^{d_v} \rightarrow \mathbb{R}^{d_u}$ . Each iteration of  $v_t \rightarrow v_{t+1}$  is defined as a combination of non-local integration operator  $\mathcal{G}$  and local nonlinear activation function  $\sigma$ . Among them, the local integration operator is formalized as:

$$(G(a; \emptyset)v_t)(x) = \int_D \mathcal{K}(x, y, a(x), a(y); \emptyset)v_t(y) dy \quad \forall x \in D \quad (1)$$

where  $D$  represents the domain of the function,  $\mathcal{K}$  represents the kernel integral operator, parameterized by  $\emptyset$ .

## 2.2. Fourier transform and Fourier neural operator

Fourier transform is a mathematical transformation. It analyzes the frequency components of a signal by decomposing it into a combination of sine and cosine waves of different frequencies, and has wide applications in many scientific and engineering fields [14, 15, 16]. In practice, it is a spectral method commonly used to solve partial differential equations [17, 18]. The specific Fourier transform and its inverse transform form are as follows:

$$F(\omega) = \int_{-\infty}^{\infty} f(t)e^{-j\omega t} dt, \quad (2)$$

$$f(t) = \frac{1}{2\pi} \int_{-\infty}^{\infty} F(\omega)e^{j\omega t} d\omega. \quad (3)$$

In the Fourier domain, differential operations become simpler because differentiation is equivalent to multiplication in the Fourier domain. This makes Fourier transform a powerful tool for solving partial differential equations, especially in cases involving frequency components. Through Fourier transform, complex differential equations can be transformed into algebraic equations that are easier to handle, thereby simplifying the solving process. Fourier transform has played an important role in the development of deep learning. In theory, Fourier transform appears in the proof of the general approximation theorem, which states that multi-layer neural networks can approximate any continuous function [19]. In practice, they are often used to accelerate convolutional neural networks [20]. Neural network architectures associated with Fourier transforms or sinusoidal activation functions are proposed and studied [21, 22, 23].

Recently, some spectral methods for partial differential equations have been extended to neural networks. A new neural operator architecture has been proposed by Li et al [7]. This architecture directly defines a kernel integration operator in Fourier space with quasi-linear time complexity and advanced approximation capabilities. This advancement opens new avenues for the application of neural networks in meshless and infinite dimensional spaces, thus enabling neural networks to efficiently handle complex partial differential equation problems.

The convolution operator is introduced in FNO to replace the kernel integration operator in Equation 1, Let  $F$  denote the Fourier transform of a function  $f : D \rightarrow \mathbb{R}^d$ , and  $F^{-1}$  its inverse, then

$$(\mathcal{F}f)_j(k) = \int_{-D}^D f_j(x) e^{-2\pi i x k} dx \quad (4)$$

And the inverse Fourier transform is given by:

$$(\mathcal{F}^{-1}f)_j(x) = \int_{-D}^D f_j(k) e^{2\pi i x k} dk \quad (5)$$

By specifying  $k(x, y, a(x), a(y)) = k(x, y)$ , and applying the convolution theorem, the Fourier kernel integral operator can be obtained:

$$K(\phi)v_t(x) = \mathcal{F}^{-1}(\mathcal{R}_\phi \cdot (\mathcal{F}v_t)(x)) \quad \forall x \in D \quad (6)$$

### 2.3. Operator Learning Methods

In the study of various partial differential equation problems, numerous operator design schemes have been proposed, yielding good results. Most operator-learning methods utilize convolutional neural networks and fully connected neural networks [24, 25, 26]. DeepONet, developed by Lu et al. [27], is based on the universal approximation theorem. The network comprises two parts, a branch network and a trunk network, which process the information from the sampled points of the input function and the target points, respectively. The outputs of these two parts are then combined to generate the final result, effectively approximating and predicting complex nonlinear operators. For the irregular grid problem, Li et al. [28] proposed the Geo-FNO model, Geo-FNO works by transforming complex geometric tasks such as point clouds into a potentially unified mesh. Use this mesh as an input to FNO to efficiently process complex geometries . Tran et al. [29]

proposed a decomposed Fourier neural operator (F-FNO), F-FNO introduces new separable spectral layers and improved residual connections, combined with training strategies such as the Markov assumption, Gaussian noise, and cosine learning rate decay, significantly reducing errors on several benchmark PDEs. Gupta et al. [30] proposed the Multi-Wavelet Transform Neural Operator (MWT), MWT takes advantage of the fine-grained representation of the Multi-Wavelet Transform and the orthogonal polynomial bases by compressing the kernel of the operator onto a Multi-Wavelet polynomial basis. A strong approximation capability is demonstrated in several PDE tasks. Zhang et al. [31] proposed a spectral neural operator(SNO), SNO converts inputs and outputs into coefficients of basis functions, learning the mapping between inputs and outputs sequentially while alleviating systematic bias caused by aliasing errors . Xiong et al. [32] proposed the Koopman Neural Operator (KNO) based on the Koopman theory. The KNO replaces the feature mapping in the Fourier Neural Operator with the Koopman Operator, which improves the performance of the FNO in long-term prediction.

In addition, there are other operator methods with deep architecture designs. Based on the U-Net concept and residual connections, multi-scale processing is performed for PDE tasks [33, 34]. For example, Zhang et al. [35] designed a U-shaped neural operator (U-NO), U-NO’s U-shaped structure improves model depth and memory efficiency. In benchmark tests for solving partial differential equations, such as Darcy’s and Navestock’s equations, U-NO significantly improves prediction accuracy. Wen et al. [36] frame-integrated FNO with U-Net to design an enhanced Fourier neural operator (U-FNO), U-FNO enhances the ability of FNO to handle multi-scale data by using residual connections. Wu et al. [37] proposed the latent spectrum model (LSM), LSM introduces a projection technique that sequentially projects high-dimensional data into multiple compact latent spaces, thereby eliminating redundant coordinate information. Based on triangular basis operators, the LSM decomposes complex nonlinear operators into multiple basis operators through neural spectral blocks, thereby enhancing the ability to solve complex partial differential equations. These novel neural operator learning methods have made significant advances and breakthroughs in various fields, demonstrating excellent performance.

### 3. Method

#### 3.1. Problem Setup

For a PDE-governed task, consider a bounded open set  $D \subset \mathbb{R}^d$  representing the coordinate domain. For this problem, inputs and outputs can be reformulated as functions defined over the coordinate domain, which belong to the Banach spaces  $X = X(D; \mathbb{R}^{dx})$  and  $Y = Y(D; \mathbb{R}^{dy})$ , where  $\mathbb{R}^{dx}$  and  $\mathbb{R}^{dy}$  denote the ranges of the input and output functions, respectively.

At each coordinate  $s \in D$ , the function values  $x(s) \in \mathbb{R}^{dx}$  and  $y(s) \in \mathbb{R}^{dy}$  represent the input and output values at location  $s$ , akin to pixel values. Under this framework, the PDE-solving process is framed as approximating the optimal mapping operator  $G : X \rightarrow Y$ , typically using a deep neural network model  $G_\theta$  to approximate this mapping, where  $\theta \in \Theta$  represents the parameter set of the model. The model learns from observed samples  $\{(x, y)\}$  to approximate  $G$ .

#### 3.2. Overall Architecture

Current mainstream neural operators usually adopt an iterative update strategy, which leads to the problem of spatial information loss due to iteration. To address this problem, we propose a parallel architecture based on hierarchical projection called Deep Parallel Neural Operator. This approach maps the data to different latent spaces, approximates the complex mapping between these latent spaces, and thus fits the overall input-output mapping. We use multiple simple and efficient parallel Fourier layer modules to learn the mapping relationships within different latent spaces by employing different combinations of modal truncations to process different frequency information.

Overall architecture: start from input  $\alpha(x)$ , Lift to a higher dimension channel space by a neural network  $P$ , Local feature extraction via  $\theta$ . The input data is mapped to the potential space by two projections, Learning the solution operator via a block of parallel Fourier layers and finally returns to the original space through a decoder, as shown in Fig 1. Specifically, the DPNO architecture is divided into three main modules:

$$G_\theta = \text{Loop} (G_{\theta_{\text{toLatentSpace}}} \circ G_{\theta_{\text{Ksolve}}} \circ G_{\theta_{\text{toOriginalSpace}}}) \quad (7)$$

where  $\circ$  denotes the sequential combination between operations. In the DPNO architecture,  $G_{\theta_{\text{toLatentSpace}}}$  denotes encoding data and mapping it to

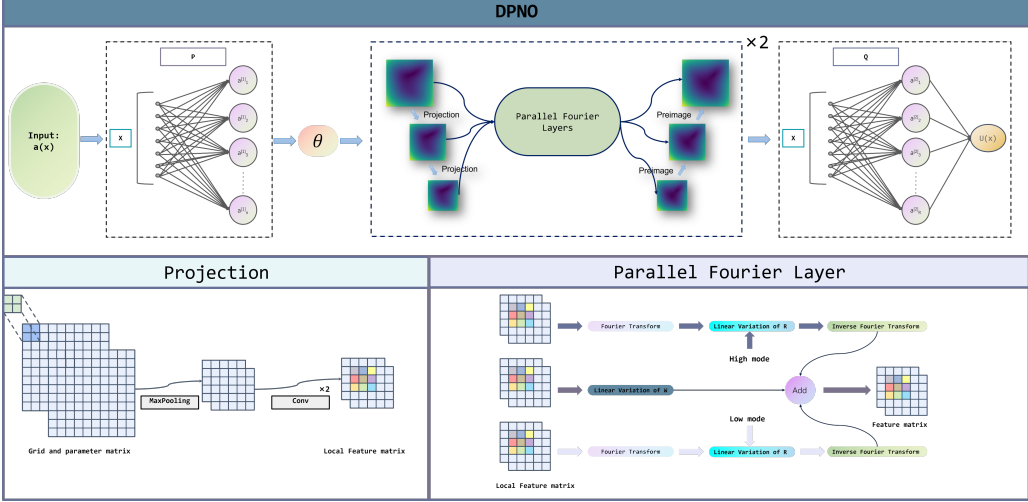


Figure 1: DPNO overall architecture

different latent spaces, and decoding  $G_{\theta_{\text{toOriginalSpace}}}$  projects the data from latent space to original space.  $G_{\theta_{\text{Ksolve}}}$  denotes a complex mapping that approximates inputs and outputs from latent space to different subspaces. ‘Loop’ denotes a Loop. To improve model efficiency and reduce the number of parameters,  $G_{\theta_{\text{Ksolve}}}$  shares the same set of parameters in the loop and learns the same set of parameters twice, i.e., the loop iterates twice.

### 3.3. Encoder

The data preprocessing of this architecture is consistent with the previous standard components for neural operators. Given an input function  $a : \mathcal{D}_A \rightarrow \mathbb{R}^{d_A}$ , first perform a dimensionality increase operation  $P$  on  $a$  to calculate  $v_0 : \mathcal{D}_A \rightarrow \mathbb{R}^{d_0}$ , where the dimensionality increase operation  $P$  is parameterized by a shallow fully connected neural network, and its function is as follows:

$$v_0(x) = P(a(x)) \quad \forall x \in \mathcal{D}_0 \quad (8)$$

where  $d_0 \gg d_A$ . Then, through a local transformation  $\phi_i$ :

$$x_1^{(L_i)} = \phi_i(v_0(x)) \quad i = 0, 1, \dots, T-1 \quad (9)$$

After the local transformations, the data are sequentially mapped to multiple potential spaces through a coding network.

The encoding network is a central part of DPNO. It maps data sequentially to multiple compact potential spatial representations. Consider that the Fourier transform is globally valid. Unlike simple downsampling methods, projection networks use classical convolutional combinations to extract local information from the data. Features are downsampled and compressed through pooling operations as a way to map to a lower dimensional space. This combination not only preserves key spatial information in the data, but also removes redundant noise. As a result, the effectiveness and expressiveness of the data representation can be enhanced while reducing the dimensionality. For the given input  $x_1^{(L_i)}$ , the projection calculation is performed to obtain  $x_2^{(L_i)} : \mathcal{D}_0 \rightarrow \mathcal{D}_1$ . The combinatorial process is formally described as:

$$x_2^{(L_i)} = T(x_1^{(L_i)}), \quad x_3^{(L_i)} = T(x_2^{(L_i)}) \quad (10)$$

Where  $i$  represents the potential space number. In our model, we map the data to three different latent spaces that contain the original space. Two sets of representations in different latent spaces are obtained by two local transformations  $\phi_i$ . These two local transformations are learnt using the same set of learnable parameter operators and projected using different learnable parameter encoding networks.

### 3.4. Parallel Fourier layer block and Decoder

With a hierarchical projection network, we map the data to different potential spaces. We use a parallel double Fourier layer to approximate the complex mapping between input and output, and since modal truncation is performed after the Fourier transform, a simple convolutional layer is used via residual concatenation to compensate for the loss of high-frequency information. The formal description is as follows:

$$G_{\theta_K} = \sum_{i=1}^N (W_{\theta_1}^i G_1^i, W_{\theta_2}^i G_2^i, R^i) \quad (11)$$

where  $i$  represents the potential space number.  $G_1^i$  and  $G_2^i$  respectively represent two parallel operators in the same latent space  $\mathcal{D}_i$ , each with learnable parameters  $W_{\theta_1}^i$  and  $W_{\theta_2}^i$ .  $R^i$  is a simple linear network. Considering the frequency aliasing caused by coding, we employ a modal grouping strategy for modal truncation in different latent spaces. Specifically, the lower the spatial dimension, the smaller the modes are, thus adapting to the frequency information aliasing error. Different modes are used to extract different Fourier

Table 1: Summary of experiment benchmarks.

Physics	Benchmark	Geometry	#DIM
SOLID	Elasticity-G	Regular Grid	2D
SOLID	Plasticity	Structured Mesh	3D
FLUID	Navier-Stokes	Regular Grid	2D
FLUID	Darcy	Regular Grid	2D
FLUID	Airfoil	Structured Mesh	2D
FLUID	Pipe	Structured Mesh	2D

blocks in the same latent space. This is because low frequency information tends to retain more physical information.

$$G_{\theta_{\text{toOriginalSpace}}} : v_{\text{out}}^i(\mathbb{R}^{d^i}) \rightarrow v_{\text{out}}^{(i')}(\mathbb{R}^{d^{(i-1)}}), \quad v_{\text{out}}^{(i-1)}(\mathbb{R}^{d^{(i-1)}}) = [v_{\text{out}}^{(i')}, v_{\text{out}}^{(i-1)}] \quad (12)$$

The operation  $v_{\text{out}}^i(\mathbb{R}^{d^i}) \rightarrow v_{\text{out}}^{(i')}(\mathbb{R}^{d^{(i-1)}})$  represents projecting the  $i$ -th latent spatial data to the  $i-1$  space through an ascending dimensional network. Merge  $v_{\text{out}}^{(i')}$  with the outputs  $v_{\text{out}}^{i-1}$  of  $i-1$  spaces. Conduct merging of adjacent latent space outputs in a sequential manner until the process returns to the original space  $\mathbb{R}^{d_0}$ .

## 4. Experiment and Results

In order to fully assess the performance of the model, we selected six partial differential equation benchmark datasets. The model relative errors were recorded. In order to reflect the superiority and generalisation ability of the model, we have selected four partial differential equations in fluid mechanics in addition to two partial differential equations related to solid mechanics. Details are given in Table 1.

### 4.1. Baselines and Settings

In order to better demonstrate the performance of our proposed model, we compare DPNO with seven currently recognized state-of-the-art models, including U-Net, FNO, WMT, U-FNO, UNO, F-FNO, and LSM. Among them, LSM is currently the best overall performer on the six datasets. We used the same experimental setup for all models. The detailed experimental setup is shown in Table 2:

Table 2: Experimental Setup.

epoch	learning_rate	optimizer
500	0.001	Adam(1e-4)

To ensure that all models converge, we set the number of training rounds to 500. Each parameter of the model will be updated using the Adam optimiser with a learning rate of 0.001 and a weight decay of 0.0001.

#### 4.1.1. Evaluation Metrics

Based on the problem setting, the whole task is to solve for one or more sets of outputs from one set of inputs. The numerical values themselves are small, so in order to describe the model performance more objectively. We use MSE as an evaluation metric.

MSE is a commonly used metric for evaluating the performance of predictive models and is used in various types of machine learning tasks. It reflects the magnitude of the model’s error by measuring the average squared difference between the model’s predicted and actual values. The smaller the value of MSE, the closer the model’s predictions are to the true values.

Given a dataset containing  $n$  samples, where each sample has an actual value  $y_i$  and a corresponding predicted value  $\hat{y}_i$ , the MSE is given by:

$$MSE = \frac{1}{n} \sum_{i=1}^n (y_i - \hat{y}_i)^2 \quad (13)$$

#### 4.2. Datasets and Results

This section will specifically describe the six datasets and show the experimental results of the proposed model and the seven baselines in this paper.

##### 4.2.1. Navier-stokes Equation

The Navier Stokes equation is a fundamental equation that describes fluid motion. Consider the two-dimensional Navier-Stokes square for a viscous, incompressible fluid on the unit ring surface, which can be described in vorticity form as:

$$\begin{aligned}
\frac{\partial \omega(x, t)}{\partial t} + u(x, t) \cdot \nabla \omega(x, t) &= \nu \Delta \omega(x, t) + f(x), \quad x \in (0, 1)^2, \quad t \in (0, T] \\
\nabla \cdot u(x, t) &= 0, \quad x \in (0, 1)^2, \quad t \in (0, T] \\
\omega(x, 0) &= \omega_0(x), \quad x \in (0, 1)^2
\end{aligned} \tag{14}$$

Among them,  $u \in C([0, T]; H_{\text{per}}^r((0, 1)^2; \mathbb{R}^2))$  for any  $r > 0$  is the velocity field,  $\omega$  is the vorticity,  $\omega_0 \in L_{\text{per}}^2((0, 1)^2; \mathbb{R})$  is the initial vorticity,  $\nu > 0$  is the viscosity coefficient,  $f \in L_{\text{per}}^2((0, 1)^2; \mathbb{R})$  is the forcing function. The main purpose of the neural network is to learn operators that map vorticity before time 10 to vorticity at some later time  $T > 10$ ,  $G : C([0, 10]; H_{\text{per}}^r((0, 1)^2; \mathbb{R})) \rightarrow C((10, T]; H_{\text{per}}^r((0, 1)^2; \mathbb{R}))$ , defined as  $\omega : (0, 1)^2$  from  $[0, 10]$  to  $(10, T]$ .

The initial condition  $w_0(x)$  is derived from  $\omega_0$ , defined as

$$w_0 = N(0.73 \cdot 2(\cos(x_1 + x_2) + 4.9i), 0.25),$$

which satisfies periodic boundary conditions. The external forcing term is fixed as

$$f(x) = 0.1(\sin(2(x_1 + x_2)) + \cos(2(x_1 + x_2))).$$

The equation is solved using a stream function representation combined with a pseudospectral approach. Initially, a Poisson equation is resolved in the Fourier domain to determine the velocity field. Subsequently, the vorticity is differentiated, and nonlinear terms are computed within the physical domain, followed by a dealiasing process to eliminate high-frequency noise. Time integration employs the Crank-Nicolson scheme, treating the linear terms implicitly while keeping the nonlinear terms explicit. For data generation, downsampling is performed to obtain a  $64 \times 64$  grid resolution for training and testing. The results are shown in Table 3. Experimental results are plotted in Appendix A.

#### 4.2.2. Plastic Problem

Consider the plastic forming problem in which a block of material  $\Omega = [0, L] \times [0, H]$  is subjected to the impact of a frictionless rigid mould at time  $t = 0$ . The mould is geometrically parameterised by an arbitrary function  $S_d \in H^1([0, L]; \mathbb{R})$  and moves with a constant velocity  $v$ . The lower edge of the block of material is clamped and the upper edge is subjected to a

Table 3: Model performance comparison on the Navier-Stokes benchmark.

Model	Navier-stokes Equation
U-Net(2015)	0.1982
geo-FNO(2023)	0.1556
WMT(2021)	0.1541
U-NO(2022)	0.1731
U-FNO(2021)	0.2231
F-FNO(2023)	0.2322
LSM(2023)	0.1535
DPNO	0.1303

displacement boundary condition. The lower edge of the material block is clamped and a displacement boundary condition is imposed on the upper edge. The elastic-plastic intrinsic model is used in this case as follows:

$$\begin{aligned} \sigma &= C : (\epsilon - \epsilon_p), \\ \dot{\epsilon}_p &= \lambda \nabla \sigma f(\sigma), \\ f(\sigma) &= \begin{cases} \sqrt{3}|\sigma - \frac{1}{3}\text{tr}(\sigma) \cdot I|F - \sigma_Y & \text{if } \lambda \geq 0, f(\sigma) \leq 0, \lambda \cdot f(\sigma) = 0, \\ 0 & \text{otherwise.} \end{cases} \end{aligned} \quad (15)$$

where the plastic multiplier is constrained by  $\lambda \geq 0$ ,  $f(\sigma) \leq 0$ , and  $\lambda \cdot f(\sigma) = 0$ . The isotropic stiffness tensor  $C$  is characterized with Young's modulus  $E = 200$  GPa and Poisson's ratio  $\nu = 0.3$ . The yield strength  $\sigma_Y$  is set to 70 MPa with the mass density  $\rho_s = 7850 \text{ kg/m}^3$ .

For this problem, we view the problem as a three-dimensional problem containing time. For neural networks, the main concern is to model the changing state of the material at a future moment through the initial state. The dataset is from the baseline model geo-FNO. Contains 980 training data and 80 test data. All data points are contained on a  $101 \times 31$  structured grid with 20 time steps [28]. The results are shown in Table 4 and Fig 2.

#### 4.2.3. Darcy Flow

Henry Darcy's law describes the flow characteristics of fluids through porous media. This law finds extensive applications across numerous natural science fields, including Fourier's law in heat conduction, Ohm's law in electric current, and Fick's law in diffusion theory. The fundamental form of

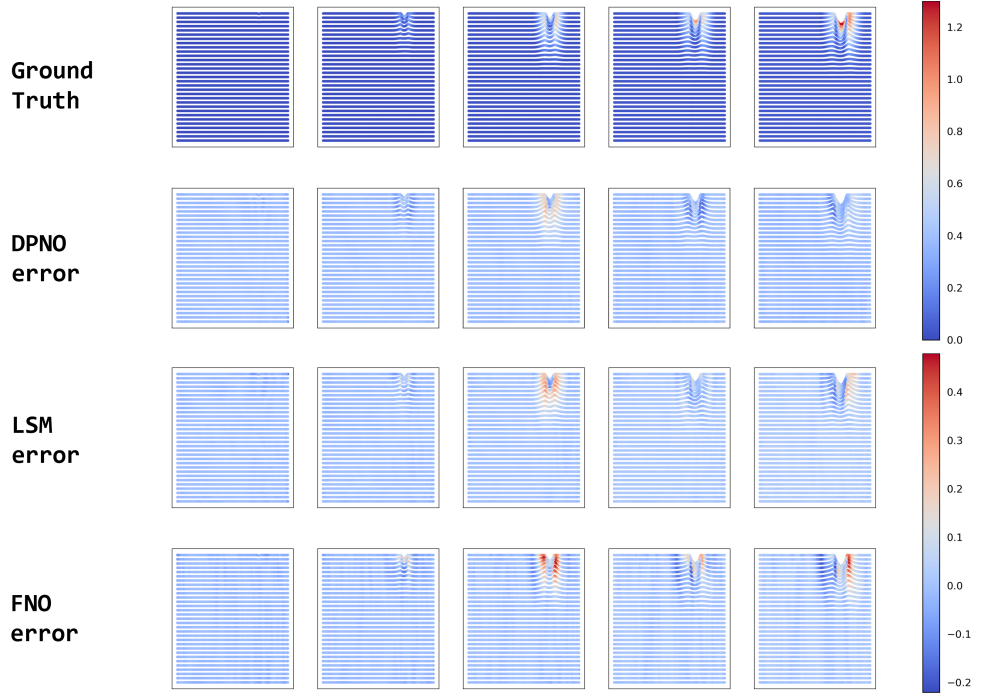


Figure 2: Plastic Problem: The first row is the true value, rows 2-4 are the model error, and on the right side are the true value legend and the error legend, respectively. Each column represents a state at a point in time.

Darcy's law is:

$$Q = -KA \frac{dh}{dl} \quad (16)$$

Where  $Q$  refers to the volume of fluid passing through the medium per unit time,  $K$  is the permeability coefficient,  $A$  is the flow cross-sectional area, and  $\frac{dh}{dl}$  is the pressure gradient. We consider the steady state of the two-dimensional Darcy flow equation in a unit rectangle. It is a second-order, linear, elliptic partial differential equation with Dirichlet boundary conditions. The format is as follows:

$$\begin{aligned} -\nabla \cdot (a(x)\nabla u(x)) &= f(x), \quad x \in (0, 1)^2, \\ u(x) &= 0, \quad x \in \partial(0, 1)^2. \end{aligned} \quad (17)$$

Table 4: Model performance comparison on the Plasticity problem benchmark.

Model	Plasticity
U-Net(2015)	0.0051
geo-FNO(2023)	0.0074
WMT(2021)	0.0076
U-NO(2022)	0.0034
U-FNO(2021)	0.0039
F-FNO(2023)	0.0047
LSM(2023)	0.0025
DPNO	0.0019

where  $a \in L((0, 1)^2; \mathbb{R}^+)$  is the diffusion coefficient and  $f \in L^2((0, 1)^2; \mathbb{R})$  is the forcing function.

For the above equation, with respect to neural networks, our main focus is on how to obtain the solution operator through the diffusion coefficient. We used the dataset provided in the baseline paper, with a grid size of 421 \* 421. Other resolutions were extracted from the highest resolution, and our experiments used a fixed resolution of 85 \* 85. The results are shown in Table 5 and Fig 3. To better demonstrate the generalization capability of the model, comparison experiments at different resolutions were added, as shown in Table 6.

Table 5: Model performance comparison on the Darcy Flow benchmark under 85\*85 resolutions.

Model	Darcy
U-Net(2015)	0.0080
geo-FNO(2023)	0.0108
WMT(2021)	0.0082
U-NO(2022)	0.0183
U-FNO(2021)	0.0183
F-FNO(2023)	0.0077
LSM(2023)	0.0065
DPNO	0.0057

Table 6: Model performance comparison on the Darcy Flow benchmark under different resolutions.

Model	141*141	211*211	421*421
FNO	0.0109	0.0109	0.0098
UNO	0.0060	0.0058	0.0057
DPNO	0.0057	0.0056	0.0052

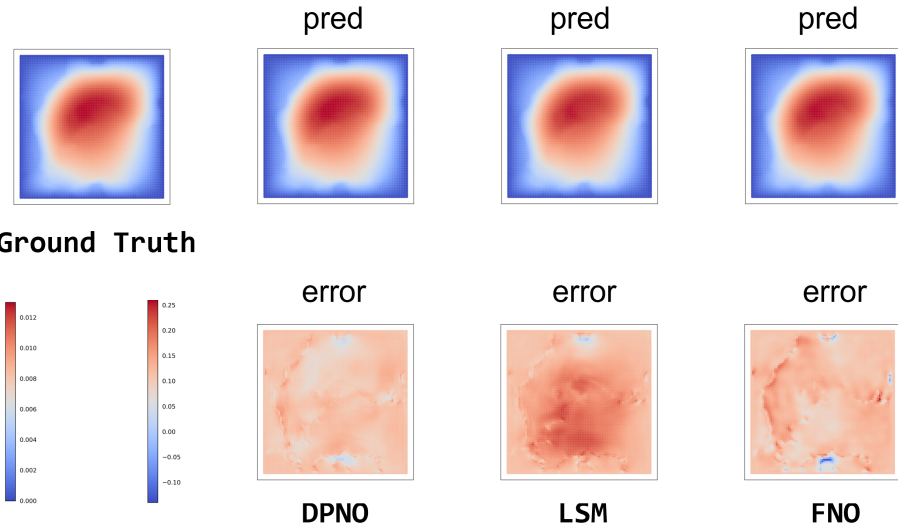


Figure 3: Darcy flow: The first row shows the true values and model predictions, the second row shows the model errors, and the legends are the true value legend and the error legend, respectively.

#### 4.2.4. Elastic Problem

The governing equations related to solid mechanics are described as follows:

$$\rho_s \frac{\partial^2 u}{\partial t^2} + \nabla \cdot \sigma = 0 \quad (18)$$

where  $\rho_s$  is the mass density,  $u$  is the displacement vector, and  $\sigma$  is the stress tensor. To complete the system, constitutive models are needed to establish the relationship between the strain tensor  $\epsilon$  and the stress tensor  $\sigma$ .

Consider a unit plane  $\Omega = [0, 1] \times [0, 1]$  with an arbitrary shaped void. The bottom of the plane is fixed, and a traction force  $t = [0, 100]$  is applied at the top. The material is the incompressible Rivlin-Saunders material. The

corresponding constitutive model for the material is given by:

$$\sigma = \frac{\partial w(\epsilon)}{\partial \epsilon} \quad (19)$$

$$w(\epsilon) = C_1(I_1 - 3) + C_2(I_2 - 3) \quad (20)$$

where  $I_1$  and  $I_2$  are scalar invariants of the right Cauchy Green stretch tensor  $C = 2\epsilon + I$ .  $C_1$  is a tunable energy density parameter. The dataset was generated by Li et al. [28] using a finite element solver with 1000 training data and 200 test data with approximately 100 quadratic quadrilateral elements. The input  $\alpha$  is given in the form of a point cloud of approximately 1000 size. Since our neural operator network is only capable of receiving uniform rectangular grid data, uniform grid data is obtained by differencing the data. The neural network mainly fits a solution operator which is able to fit the strain of the material through the initial state of the material. In the experiments, we adopted 1000 training points and 200 testing points. The results are shown in Table 7 and Fig 4.

Table 7: Model performance comparison on the Elastic Problem benchmark.

Model	Elastic-G
U-Net(2015)	0.0531
geo-FNO(2023)	0.0508
WMT(2021)	0.0520
U-NO(2022)	0.0469
U-FNO(2021)	0.0480
F-FNO(2023)	0.0475
LSM(2023)	0.0408
DPNO	0.0375

#### 4.2.5. Airfoil problem with Euler's equation.

The Airfoil Problem can be analyzed using Euler's equations, which describe the motion of an inviscid (non-viscous) fluid. These equations are a simplified form of the Navier-Stokes equations and are applicable to the flow around airfoils at high speeds where viscous effects are negligible. Euler's equations can be described as follows:

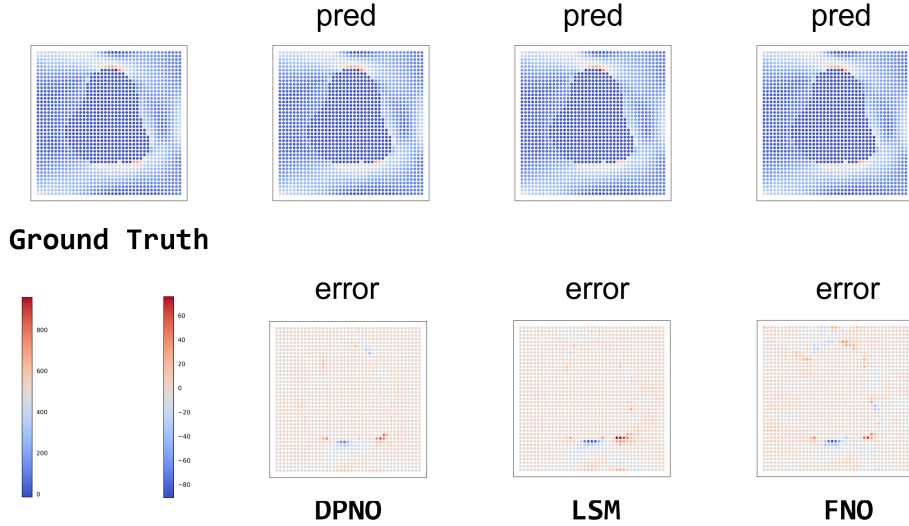


Figure 4: Elastic Problem: The first row shows the true values and model predictions, the second row shows the model errors, and the legends are the true value legend and the error legend, respectively.

$$\frac{\partial \rho}{\partial t} + \nabla \cdot (\rho \mathbf{u}) = 0 \quad (21)$$

$$\frac{\partial(\rho \mathbf{u})}{\partial t} + \nabla \cdot (\rho \mathbf{u} \otimes \mathbf{u}) + \nabla p = 0 \quad (22)$$

$$\frac{\partial E}{\partial t} + \nabla \cdot (E \mathbf{u}) + p \nabla \cdot \mathbf{u} = 0 \quad (23)$$

where  $\rho$  is the mass per unit volume, reflecting the concentration of the fluid;  $\mathbf{u}$  is the distance travelled by a fluid particle per unit time, a vector describing the change in fluid momentum and flow characteristics;  $p$  is the force acting per unit area; and  $E$  is the total energy of the system. In this case, the far-field boundary conditions are  $\rho_1 = 1$ ,  $p_1 = 1.0$ ,  $M_1 = 0.8$ , and  $\text{AoA} = 0$ , where  $M_1$  is the Mach number and  $\text{AoA}$  is the angle of attack. Additionally, a no-penetration condition is imposed at the airfoil. The dataset was generated from 1000 training data and 200 test data using a second-order implicit finite volume solver by Li et al. A C-mesh with about 200 quadrilateral elements was used and adjusted for the mesh near the wing

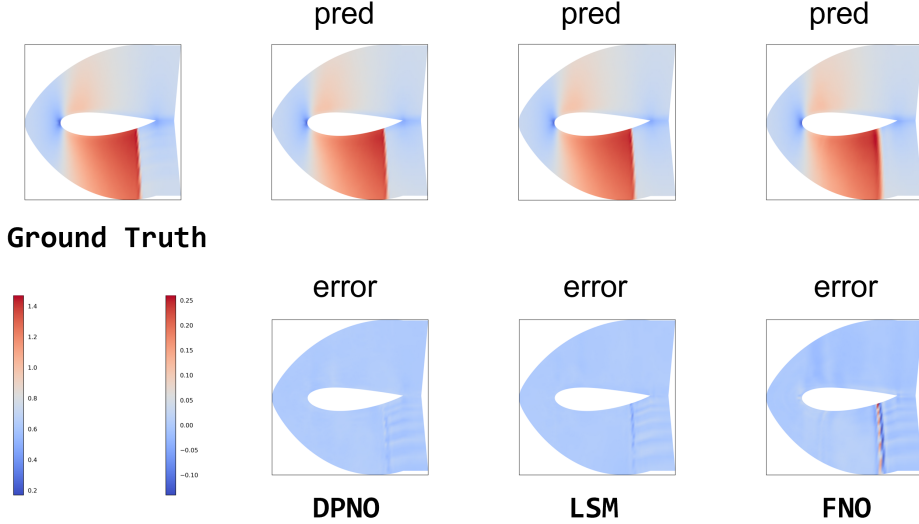


Figure 5: Airfoil problem: The first row shows the true values and model predictions, the second row shows the model errors, and the legends are the true value legend and the error legend, respectively.

but not around the impact [28]. The neural network fits a mapping from the shape parameters of the airfoil to the flow field around the airfoil. The mesh point locations and Mach number on these mesh points are used as input and output data. The results are shown in Table 8 and Fig 5.

#### 4.2.6. Pipe problem with Navier-Stokes equation

The Pipe Problem in fluid dynamics typically refers to the study of fluid flow through a pipe, governed by the Navier-Stokes equations. In the context of the pipe problem, the Navier-Stokes equations can be simplified under the assumption of steady, incompressible, and laminar flow. The simplified forms are as follows:

$$\nabla \cdot \mathbf{v} = 0 \quad (24)$$

$$\frac{\partial \mathbf{v}}{\partial t} + (\mathbf{v} \cdot \nabla) \mathbf{v} = -\nabla p + \nu \nabla^2 \mathbf{v} \quad (25)$$

where  $\mathbf{v}$  is the velocity vector,  $p$  is the pressure, and  $\nu = 0.005$  is the viscosity. In this case, at the inlet, a parabolic velocity profile is established

Table 8: Model performance comparison on the Airfoil Problem benchmark.

Model	Airfoil
U-Net(2015)	0.0079
geo-FNO(2023)	0.0138
WMT(2021)	0.0075
U-NO(2022)	0.0078
U-FNO(2021)	0.0269
F-FNO(2023)	0.0078
LSM(2023)	0.0059
DPNO	0.0054

with a maximum velocity of  $\mathbf{v} = [1; 0]$ . The outlet is treated with a free boundary condition, while the pipe surface is subject to a no-slip boundary condition. The pipe has a length of 10 and a diameter of 1. The centerline of the pipe is defined using four piecewise cubic polynomials, which are derived from the vertical positions and slopes at five evenly spaced control nodes. The vertical positions at these nodes follow a uniform distribution  $d \sim U[-2; 2]$ , and the slopes at these nodes are also distributed uniformly,  $d \sim U[-1; 1]$  [28]. The experiment uses 1000 training mesh points and 200 test mesh points. For this problem, neural networks are mainly concerned with how to model the velocity field of a fluid through geometric parameters. Grid point location parameters (129\*129) and horizontal velocity on these mesh points are used as input and output data. The results are shown in Table 9 and Fig 6.

Table 9: Model performance comparison on the Pipe Problem benchmark.

Model	Pipe
U-Net(2015)	0.0065
geo-FNO(2023)	0.0067
WMT(2021)	0.0077
U-NO(2022)	0.0100
U-FNO(2021)	0.0056
F-FNO(2023)	0.0070
LSM(2023)	0.0050
DPNO	0.0052

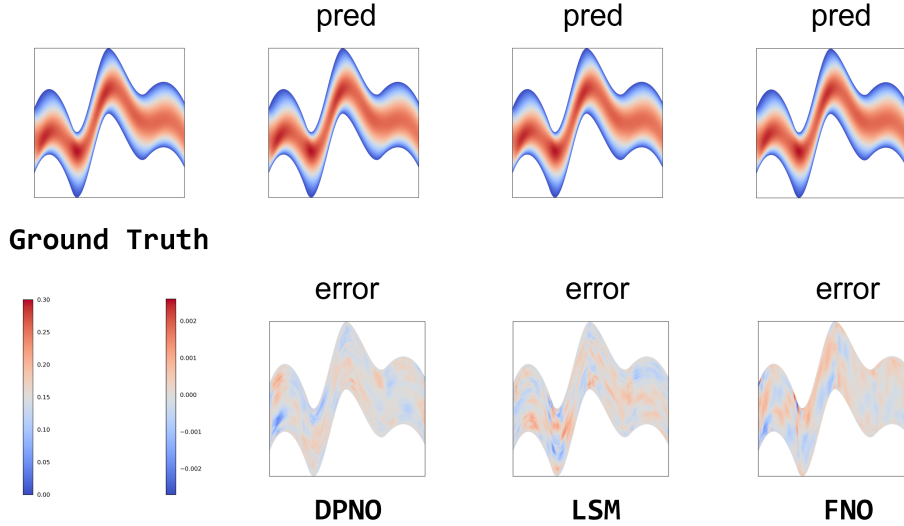


Figure 6: Pipe Problem: The first row shows the true values and model predictions, the second row shows the model errors, and the legends are the true value legend and the error legend, respectively.

#### 4.3. Results and Discussion

DPNO achieved state-of-the-art performance on five benchmark datasets and one sub-optimal. An average improvement of 11.6% is achieved compared to the overall best performing LSM. This demonstrates the versatility and excellent performance of the proposed DPNO in different PDE tasks. Compared to the baseline model FNO, DPNO shows an average performance improvement of 40% on the six datasets. Among them, the performance of the PLAYCITY-3d problem is improved by 73%. As shown in table 10: The comparison chart of model training errors stability can be found in Appendix B.

#### 4.4. Ablation Experiment

In order to verify the effectiveness of the parallel strategy in the model, we design a set of ablation experiments to change the parallel block into serial block and observe the performance changes. Specifically, we merge the parallel block horizontally into serial block as shown in Fig 7.

Due to the unidirectional nature of the serial, taking too small a modal truncation factor can lead to too much lost information, therefore, Serial

Table 10: Comparison of MSE for the 7 benchmark models on the 6 benchmark datasets. The best performing models are in bold, and the next best models are underlined. Promotion refers to the relative error reduction w.r.t. the second best model on each benchmark.

Model	Pipe	Airfoil	Elastic-G	Plasticity	Darcy	NS
U-Net(2015)	0.0065	0.0079	0.0531	0.0051	0.0080	0.1982
geo-FNO(2023)	0.0067	0.0138	0.0508	0.0074	0.0108	0.1556
WMT(2021)	0.0077	0.0075	0.0520	0.0076	0.0082	0.1541
U-NO(2022)	0.0100	0.0078	0.0469	0.0034	0.0183	0.1731
U-FNO(2021)	0.0056	0.0269	0.0480	0.0039	0.0183	0.2231
F-FNO(2023)	0.0070	0.0078	0.0475	0.0047	0.0077	0.2322
LSM(2023)	<b>0.0050</b>	<u>0.0059</u>	<u>0.0408</u>	<u>0.0025</u>	<u>0.0065</u>	<u>0.1535</u>
DPNO	<b>0.0052</b>	<b>0.0054(8.5%)</b>	<b>0.0375(8%)</b>	<b>0.0020(20%)</b>	<b>0.0057(12.3%)</b>	<b>0.1303(15%)</b>

Fourier blocks use the same modal truncation coefficients for both Fourier layers. Low frequency information tends to carry more physical information, The parallel Fourier block utilises a decreasing strategy for the modal truncation coefficients, this is due to the consistency of the inputs to each Fourier layer, changes in the modal truncation coefficients do not affect the respective learning process. The experimental results are shown in Table 11:

Table 11: Comparison of MSE for DPNO/P and DPNO on the 6 benchmark datasets. The improvement percentage is included in the DPNO row.

Model	Pipe	Airfoil	Elasticity-G	Plasticity	Darcy	NS	Total
DPNO/P	0.0059	0.0061	0.0384	0.0021	0.0069	0.1586	-
DPNO	0.0052	0.0054	0.0375	0.0020	0.0057	0.1303	10.8%

Through the ablation experiments, we can find that parallelisation has some degree of impact on the overall model performance, with an average performance improvement of 10.8%. This is because by parallelising the module, we mitigate the error accumulation caused by the iterations.

## 5. Conclusions

Neural operators are good learners when it comes to functional spaces. In this paper, we propose a deeply parallel Fourier neural operator to address the problem of error accumulation during FNO iterations. The data are projected into various potential spaces and learnt in an end-to-end manner through multiple parallel operator blocks. Excellent performance is achieved on six benchmark datasets for partial differential equations. An average improvement of 40% is achieved compared to the baseline model FNO.

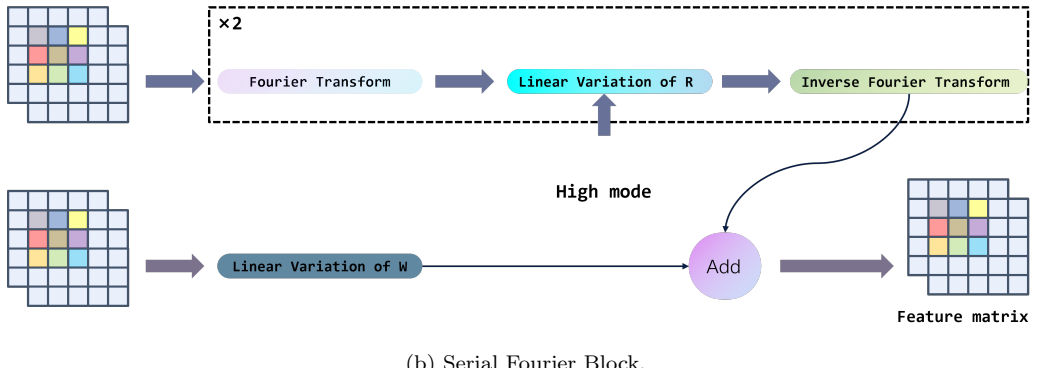
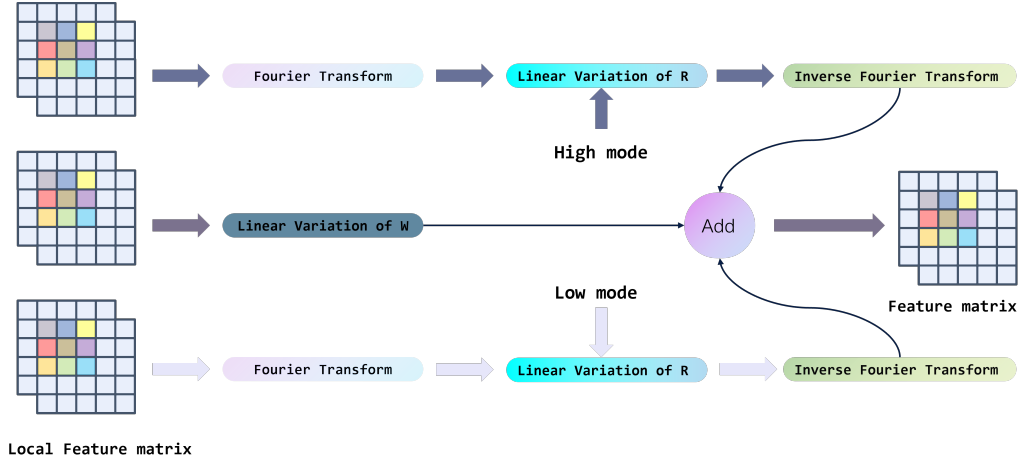


Figure 7: Comparison of Fourier Block Architectures.

Although the field of deep learning currently has good progress in learning partial differential equations. However, there are still shortcomings in long time prediction. The time dependence cannot be captured better. For dynamically changing systems, deep learning models may need to be constantly updated and retrained to adapt to new conditions. Therefore, future work tends to enhance the neural operator model by integrating the physical information model. By integrating physical information, the data dependency of the neural operator model is reduced.

## Appendix A. Navier-stokes Experiment

The following is a visualisation of the experimental results for different models on the N-S equation, as shown in Figs A.8.

Where the first row represents the true value, the second row is the model predicted value and the third row is the error. Each column corresponds to a point in time.

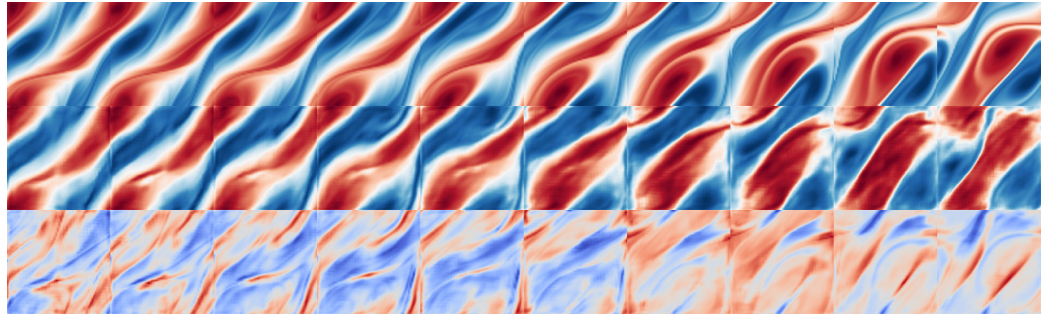


Figure A.8: Experimental results on Navier-stokes Equation.

## Appendix B. Training Stability

We provide the training error curves of the model on different benchmarks in Fig B.9. From Fig B.9, we can see that in addition to maintaining state-of-the-art performance on all benchmarks, there is comparable training stability and convergence speed compared to the SOTA model LSM and the recognised FNO.

In addition, for one experiment, we repeated the experiment at least five times or more, and all errors were within 0.0005.

## References

- [1] Gockenbach M S, *Partial differential equations: analytical and numerical methods*, Society for Industrial and Applied Mathematics, 2010.
- [2] Tanabe H, *Functional analytic methods for partial differential equations*, CRC Press, 2017.

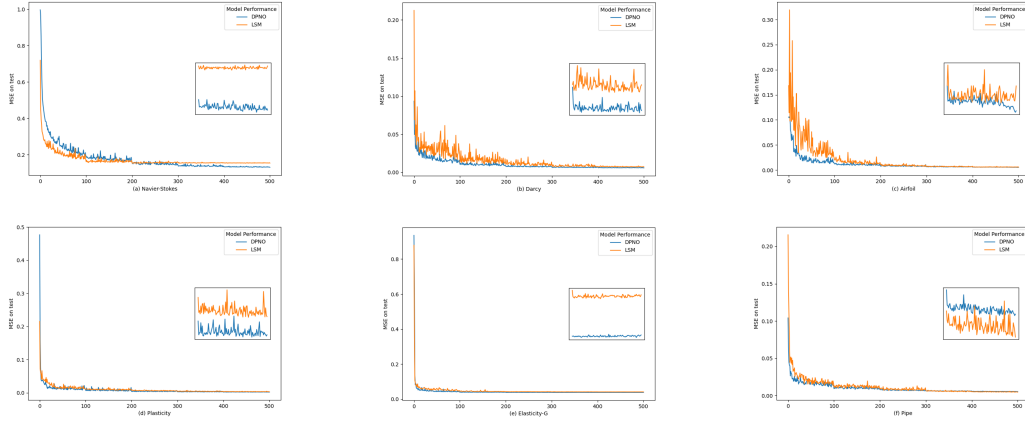


Figure B.9: Model training curves, where the x-axis means the number of epochs and the y-axis is MSE performance in the test set. The inset on the right shows a zoomed-in view of the training after 400 epochs.

- [3] Raissi, M., Perdikaris, P., Karniadakis, G. E., *Physics-informed neural networks: A deep learning framework for solving forward and inverse problems involving nonlinear partial differential equations*, Journal of Computational Physics, 378, 686-707, 2019.
- [4] Jiang, C. M., Esmaeilzadeh, S., Azizzadenesheli, K., Kashinath, K., Mustafa, M., Tchelepi, H. A., Marcus, P., Anandkumar, A., et al., *Mesh-freeFlowNet: A physics-constrained deep continuous space-time super-resolution framework*, arXiv preprint, arXiv:2005.01463, 2020.
- [5] Greenfeld, D., Galun, M., Basri, R., Yavneh, I., Kimmel, R., *Learning to optimize multigrid PDE solvers*, In International Conference on Machine Learning, PMLR, 2019, pp. 2415–2423.
- [6] Kochkov, D., Smith, J. A., Alieva, A., Wang, Q., Brenner, M. P., Hoyer, S., *Machine learning accelerated computational fluid dynamics*, arXiv preprint, arXiv:2102.01010, 2021.
- [7] Li, Z., Kovachki, N., Azizzadenesheli, K., Liu, B., Bhattacharya, K., Stuart, A., Anandkumar, A., *Fourier neural operator for parametric partial differential equations*, arXiv preprint arXiv:2010.08895, 2020.
- [8] Lim, B., Zohren, S., *Time-series forecasting with deep learning: A sur-*

vey, Philosophical Transactions of the Royal Society A: Mathematical, Physical and Engineering Sciences, 379(2194), 2021.

- [9] He, Q., Xu, W., Zhang, T., *Composite materials microstructure–property modeling using machine learning*, Advanced Materials, 33(50), 2104146, 2021.
- [10] Boyd, J. P., *Chebyshev and Fourier Spectral Methods*, Dover Publications, 2000.
- [11] Rafiq, M., Rafiq, G., Jung, H. Y., et al., *SSNO: Spatio-spectral neural operator for functional space learning of partial differential equations*, IEEE Access, 2022, 10: 15084-15095
- [12] Li, Z., Kovachki, N., Azizzadenesheli, K., et al., *Neural operator: Graph kernel network for partial differential equations*, arXiv preprint, arXiv:2003.03485, 2020.
- [13] Kovachki, N., Li, Z., Liu, B., et al., *Neural operator: Learning maps between function spaces with applications to PDEs*, Journal of Machine Learning Research, 2023, 24(89): 1-97.
- [14] Kar, C., Mohanty, A. R., *Vibration and current transient monitoring for gearbox fault detection using multiresolution Fourier transform*, Journal of Sound and Vibration, 2008, 311(1-2): 109-132.
- [15] Sandryhaila, A., Moura, J. M. F., *Discrete signal processing on graphs: Graph Fourier transform*, in Proceedings of the 2013 IEEE International Conference on Acoustics, Speech and Signal Processing, IEEE, 2013, pp. 6167-6170.
- [16] Candès, E. J., Romberg, J., Tao, T., *Robust uncertainty principles: Exact signal reconstruction from highly incomplete frequency information*, IEEE Transactions on Information Theory, 2006, 52(2): 489-509.
- [17] Canuto, C., *Spectral Methods: Evolution to Complex Geometries and Applications to Fluid Dynamics*, Springer-Verlag, 2007.
- [18] Boyd, J. P., *Chebyshev and Fourier Spectral Methods*, Courier Corporation, 2001.

- [19] Hornik, K., Stinchcombe, M., White, H., et al., *Multilayer feedforward networks are universal approximators*, Neural Networks, 2(5):359–366, 1989.
- [20] Mathieu, M., Henaff, M., LeCun, Y., *Fast training of convolutional networks through FFTs*, 2013.
- [21] Bengio, Y., LeCun, Y., et al., *Scaling learning algorithms towards AI*, Large-scale Kernel Machines, 34(5):1–41, 2007.
- [22] Sitzmann, V., Martel, J. N. P., Bergman, A. W., Lindell, D. B., Wetzstein, G., *Implicit neural representations with periodic activation functions*, arXiv preprint, arXiv:2006.09661, 2020.
- [23] Mingo, L., Aslanyan, L., Castellanos, J., Diaz, M., Riazanov, V., *Fourier neural networks: An approach with sinusoidal activation functions*, 2004.
- [24] Krizhevsky, A., Sutskever, I., Hinton, G. E., *ImageNet classification with deep convolutional neural networks*, Advances in Neural Information Processing Systems, 2012, 25.
- [25] He, K., Zhang, X., Ren, S., Sun, J., *Deep residual learning for image recognition*, In *Proceedings of the IEEE Conference on Computer Vision and Pattern Recognition*, 2016, pp. 770-778.
- [26] Hinton, G., Deng, L., Yu, D., et al., *Deep neural networks for acoustic modeling in speech recognition: The shared views of four research groups*, IEEE Signal Processing Magazine, 29(6), 82-97, 2012.
- [27] Lu, L., Jin, P., Karniadakis, G. E., *DeepONet: Learning nonlinear operators for identifying differential equations based on the universal approximation theorem of operators*, arXiv preprint, arXiv:1910.03193, 2019.
- [28] Li, Z., Huang, D. Z., Liu, B., et al., *Fourier neural operator with learned deformations for PDEs on general geometries*, Journal of Machine Learning Research, 24(388): 1-26, 2023.
- [29] Tran, A., Mathews, A., Xie, L., Ong, C. S., *Factorized Fourier neural operators*, In ICLR, 2023.
- [30] Gupta, G., Xiao, X., Bogdan, P., *Multiwavelet-based operator learning for differential equations*, In NeurIPS, 2021.

- [31] Fanaskov, V., Oseledets, I., *Spectral neural operators*, arXiv preprint, arXiv:2205.10573, 2022.
- [32] Xiong, W., Huang, X., Zhang, Z., Deng, R., Sun, P., Tian, Y., *Koopman neural operator as a mesh-free solver of non-linear partial differential equations*, arXiv preprint, arXiv:2301.10022, 2023a.
- [33] Ronneberger, O., Fischer, P., Brox, T., *U-net: Convolutional networks for biomedical image segmentation*, In *Medical Image Computing and Computer-Assisted Intervention–MICCAI 2015: 18th International Conference, Munich, Germany, October 5–9, 2015, Proceedings, Part III 18*, Springer International Publishing, 2015, pp. 234–241.
- [34] Szegedy, C., Ioffe, S., Vanhoucke, V., et al., *Inception-v4, inception-resnet and the impact of residual connections on learning*, In *Proceedings of the AAAI Conference on Artificial Intelligence*, 2017, 31(1).
- [35] Rahman, M. A., Ross, Z. E., Azizzadenesheli, K., *U-NO: U-shaped neural operators*, arXiv preprint, arXiv:2204.11127, 2022.
- [36] Wen, G., Li, Z.-Y., Azizzadenesheli, K., Anandkumar, A., Benson, S. M., *U-FNO - An enhanced Fourier neural operator based deep learning model for multiphase flow*, arXiv preprint, arXiv:2109.03697, 2021.
- [37] Wu, H., Hu, T., Luo, H., et al., *Solving high-dimensional PDEs with latent spectral models*, arXiv preprint, arXiv:2301.12664, 2023.